Corrosion Behavior of GH4169 Alloy under Alternating Oxidation at 900 °C and Solution Immersion

Zhongfen Yu [1,2]**, Li Liu** [2,3,]*****, Rui Liu** [2] **, Min Cao** [2]**, Lei Fan** [2]**, Ying Li** [2]**, Shujiang Geng** [1] **and Fuhui Wang** [3]

[1] School of metallurgy, Northeastern University, Shenyang, 110819, China; zfyu12s@imr.ac.cn (Z.Y.); gengshujiang@mail.neu.edu.cn (S.G.)

[2] Institute of Metal Research, Chinese Academy of Sciences, Shenyang 110016, China; rliu15s@imr.ac.cn (R.L.); mcao12s@imr.ac.cn (M.C.); fanlei1@cnpc.com.cn (L.F.); liying@imr.ac.cn (Y.L.)

[3] Key Laboratory for Anisotropy and Texture of Materials (MoE), School of Materials Science and Engineering, Northeastern University, Shenyang 110819, China; wangfh@imr.ac.cn

***** Correspondence: liuli@mail.neu.edu.cn; Tel.: +86-24-8108-3918; Fax: +86-24-2392-5323

check for updates

Abstract: In this paper, the corrosion behavior of GH4169 superalloy under alternating oxidation (at 900 °C) and solution immersion (in 3.5% NaCl solution, 30 ± 1 °C) has been studied by SEM, XRD, XPS, and electron probe microanalysis (EPMA). The results show that the alternating environment increases the corrosion rate of GH4169. The reaction of NaCl and Cr_2O_3 generates various volatile and soluble corrosion products, such as $Na_2Cr_2O_7$, $CrCl_3$, Cl_2, and Na_2CrO_4, at a high temperature. The destruction of the protective Cr_2O_3 film leads to the increase of defects in the oxide scale, promoting the formation of oxides, such as NiO and Fe_2O_3, and changes the composition and structure of the oxide film. After repeated iterations, the mixed oxides will result in the spalling of the oxide film because they can reduce the fracture toughness of the corrosion scale. Therefore, the corrosion is comprehensively intensified.

Keywords: Ni-based superalloy; high temperature oxidation

1. Introduction

Ni-based superalloys are widely used in the turbine blades of gas turbines and aircraft engines due to their excellent mechanical strength and oxidation resistance [1–3]. These materials, however, suffer serious corrosion in filed experiences [4–6]. Many researchers have focused on the high temperature oxidation behavior of Ni-based superalloy in pure O_2 or air [7–10]. Previous investigations showed that the GH202 superalloy had excellent oxidation resistance at 800 °C and 900 °C due to the formation of a continuous and dense Cr_2O_3 layer, which improved the bonding strength between the oxide scale and the substrate [11]. Some scholars believe that the spalling of $NiCr_2O_4$ spinel could lead to the depletion of Cr, and therefore, metals cannot form a continuous protective Cr_2O_3 layer for a long time [11].

The thermal shock resistance of nickel-based alloys was conducted by simulating the oxidation behavior under the operation and parked state of gas turbines. Studies revealed that Superni76, Superni750, and In600 had an excellent resistance to cyclic oxidation since a protective oxide scale consisting of Cr_2O_3 could form at 750 to 950 °C [12,13]. However, some researchers believed that the $NiCr_2O_4$ oxide film, resulting from the solid-state reaction between NiO and Cr_2O_3, is easily peeled off from the substrate under the cyclic oxidation, because of the high growth stress at 900 °C [14]. Besides the long time oxidation and cyclic oxidation, Ni-based alloys used in gas turbines also face

other corrosion, especially salt corrosion [15,16]. When gas turbines are used in marine environments and thermal power conditions, the hot corrosion behavior of the Ni-based superalloys in a high temperature environment containing salt is one important issue. It was found that Na_2SO_4 could provide SO_3 and O^{2-} at high temperatures, which led to the formation of MS_x and MO_x^{y-}, promoting cracking and peeling off of the oxide film, and finally accelerated corrosion [17,18]. On the other hand, Cl^- could react with metals and oxides, and form MO_x^{y-} and Cl_2 at high temperatures. Cl_2 could penetrate into the inside of the oxide film easily and further react with the oxides, leading to the peeling off of oxide films, and accelerating the corrosion of the alloy [19–21].

As previous studies usually focused on the corrosion behavior of superalloys in a single environment, a more intensive study concerning the environmental details and their relationships with the corrosion of aircraft engine blades is urgently required. In fact, engine blades are used in elevated temperatures and high salt environments in the marine environment during operation and parking, respectively. In this environment, the blade suffers synergistic corrosion between high oxidation and low temperature electrochemical reactions. When working in high temperatures, oxidation happens; on the other hand, when parked in normal temperatures, the electrochemical reaction happens. Therefore, the metal materials used in aircraft engine blades experience a special corrosion: An alternating high temperature oxidation and normal temperature electrochemical reaction. However, limited published papers have focused on these alternating oxidation and electrochemical reactions.

In this paper, the alternating corrosion behavior of GH4169 alloy (the blade material) under the alternating high-temperature oxidation (900 °C) and normal temperature corrosion (3.5% NaCl solution, 30 ± 1 °C) were investigated. The corrosion rate was calculated by weighing experiments, and the composition and morphology of the corrosion products were analyzed by XRD, XPS, and SEM. The alternating corrosion mechanism was discussed.

2. Materials and Methods

2.1. Material and Specimens

The material used in this study was Ni-based superalloy GH4169, with a chemical composition as listed in Table 1. After cut into a piece with the dimensions of 10 mm × 10 mm × 2 mm, the specimens were ground using SiC papers up to 2000 grit, cleaned with distilled water and alcohol, and dried in cold air before the corrosion tests.

Table 1. The compositions of GH4169 alloy.

Element	C	Cr	Mo	Al	Ti	Fe	Nb + Ta	B	Ni
Mass%	0.045	19.09	3.25	0.88	0.83	18	5.08	0.05	Bal.

2.2. Alternating Oxidation and Normal Temperature Corrosion Test

The specimens were suspended by a quartz and inserted inside a tube furnace, in which it was first performed in static air conditions at 900 °C for 10 h. After 10 h of oxidation, these specimens were cooled down in the air to room temperature for 1 h and immersed in a 3.5% NaCl solution at 30 ± 1 °C for another 10 h. Then, the specimens were dried with hot air for 15 min and NaCl was deposited evenly on the surface of the specimens. Next, the specimens were put into the tube furnace to begin the next experimental cycles. Each experimental cycle was 20 h, including 10 h of oxidation and 10 h of normal immersion in 3.5% NaCl solution. The whole test included 10 cycles, as shown in Figure 1. Specimens after high temperature corrosion were recorded as No. x. 5 cycle (x is the number of cycles, x = 0, 1, 2, ... 10, the same below), and those after normal temperature corrosion were recorded as No. x cycle.
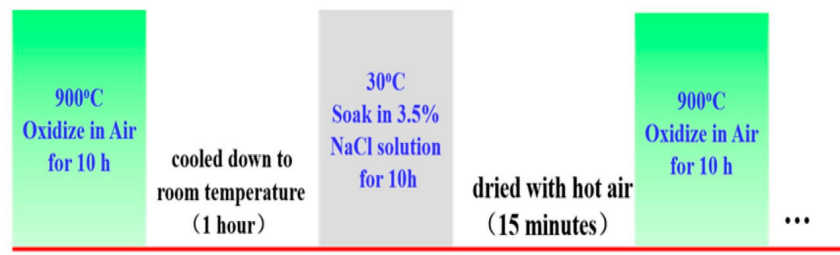
Figure 1. Schematic of the experimental cycles: alternating oxidation (at 900 °C) and solution emersion (in 3.5% NaCl solution, 30 ± 1 °C).

After each half cycle, all the samples were weighed using an electronic balance with an accuracy of 0.01 mg. There were five parallel samples in each weighing experiment. To ensure reasonable reproducibility, all the weight gain tests were normally repeated at least four times for each specimen. Each experiment was repeated at least three times. The surface morphology of the NaCl deposit is shown in Figure 2, which shows that the NaCl layer is uniform over the surface of the specimen. The average weight of the NaCl deposit was about 0.1mg/cm^2.
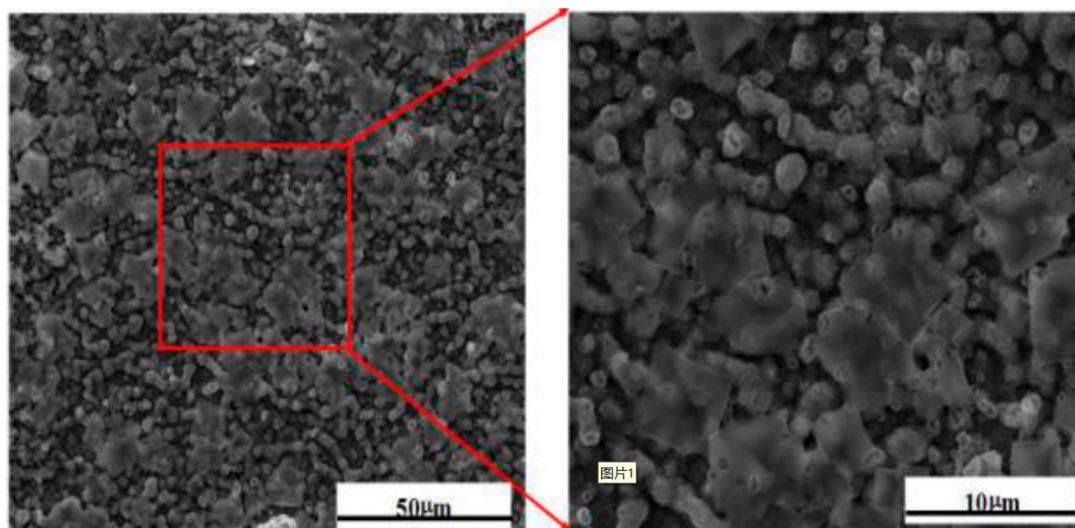

Figure 2. Surface morphology (SEM, SEI) of the NaCl deposit on the surface of the oxide scale after No. 0.5 and 1 cycles (oxidation at 900 °C and emersion in 3.5% NaCl solution).

2.3. Experimental Methods

The surface and cross-section morphologies of the oxides were observed by a field emission scanning electron microscope (SEM) (FEI INSPEWCT F50, Hillsboro, OR, USA) equipped with an energy dispersive spectrometer (EDS) (INCA, X-Max, Oxford instruments Co., Oxford, UK). The acceleration voltage of the applied scanning electron microscope is 25 kV, both of which used secondary electron images (SEI) and backscattered electron images (BEI).

The distribution of the elemental elements of the oxide film was detected by an electron probe micro analyzer (EPMA). The EPMA equipment was a Shimadzu Model EPMA-1610 electron probe micro analyzer (Kyoto, Japan) at a 15 kV accelerated voltage.

X-ray diffraction (XRD, X'pert PRO, Panalytical, Almelo, The Netherlands) was used to determine the phase composition of the oxide film. A step-scanning X-ray diffractometer was utilized, with Cu Kα radiation, in the scanning range of 10 to 90°.

The valence composition of the chemical elements in the corrosion products was examined by an ESCALAB 250 X-ray photoelectron spectroscopy (XPS, Waltham, MA, USA). Al Kα1486.6 eV was

chosen as the monochromatic X-ray source. The light was 500 μm in diameter, and the pass energy was 50 eV. The binding energy of the carbon adsorption energy calibration was 284.6 eV.

3. Results

3.1. Kinetics of Hot Corrosion

Figure 3 shows the weight gain curve of the sample under alternating corrosion tests. The results show that the mass gain was only obtained after the first cycle, including the 0.5 cycle and 1cycle. After the other cycles, the weight of the specimens decreased, thus the weight loss was obtained for the remaining experimental cycles. Additionally, the weight loss increased with the increasing cycle number. The weight loss increased up to 52.8 ± 2.1 mg/cm^2 of the No.10 cycle. In addition, weight loss occurred in both the oxidation at 900 °C and normal immersion at 30 °C from the No.1.5 cycle to the No.10 cycle.
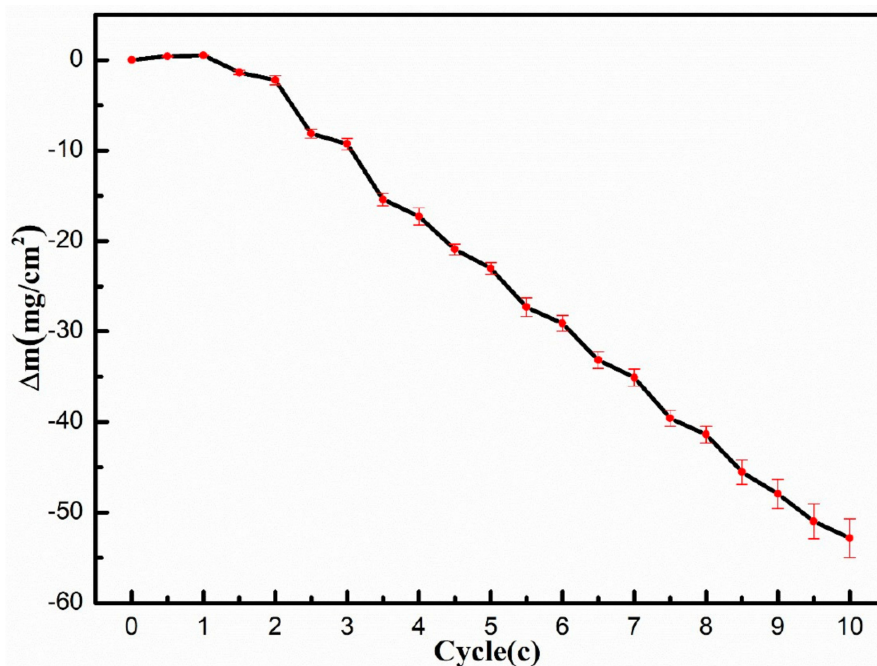

Figure 3. Weighing curve of GH4169 in 10 cycles of a high and low temperature alternating environment (oxidation at 900 °C and emersion in 3.5% NaCl solution).

3.2. XRD Analyses

The compositions of the corrosion products after different cycles were analyzed by XRD. The XRD analysis revealed the corrosion products and matrix information of samples after different cycles, as shown in Figure 4. The result shows that, except the matrix information, the corrosion products consisted of Cr_2O_3 and $CrNbO_4$ after the No. 0.5 cycle. It indicates that an oxide layer mainly composed of Cr_2O_3 formed on the surface of the material after the 900 °C oxidation. From the XRD results, $CrNbO_4$ in the oxide film was converted to $Nb_{0.6}Cr_{0.4}O_2$ after the No. 1.5 cycle. In fact, after the 1.5 cycle, the corrosion products were not compact and loose because we also measured the corrosion product powders filtered from the 3.5% NaCl solution after two cycles, as shown in Figure 4. We noticed that the corrosion products on the samples were mainly Cr_2O_3 and Cr-Nb oxides after two cycles. Additionally, some powders remained in the immersion solution. We filtered them and tested them. We found that the remaining powders were the corrosion products formed on the samples. They were still Cr_2O_3 and Cr-Nb oxides. This result indicates that after the 1.5 cycle, although Fe and Ni oxides did not form, the corrosion products filled with Cr_2O_3 and Cr-Nb oxides are not compact, like that formed after the 0.5 cycle. Corrosion products can peel off in the immersion solution.

In the XRD of the corrosion product powders, there is no matrix information. When the specimen was oxidized after the 2.5 cycle, new oxides, such as NiO, Fe_2O_3, and $NiCr_2O_4$, were detected by XRD analysis. From the No. 2.5 cycle to the No. 9.5 cycle, the phase composition of the corrosion products' film changed slightly while a weakened intensity of the peak of Cr_2O_3 was detected, suggesting a decrease of the Cr_2O_3 content. The XRD results show the change of the corrosion products. From the initial main Cr_2O_3 layer, the corrosion products changed to be NiO, Fe_2O_3, and $NiCr_2O_4$.
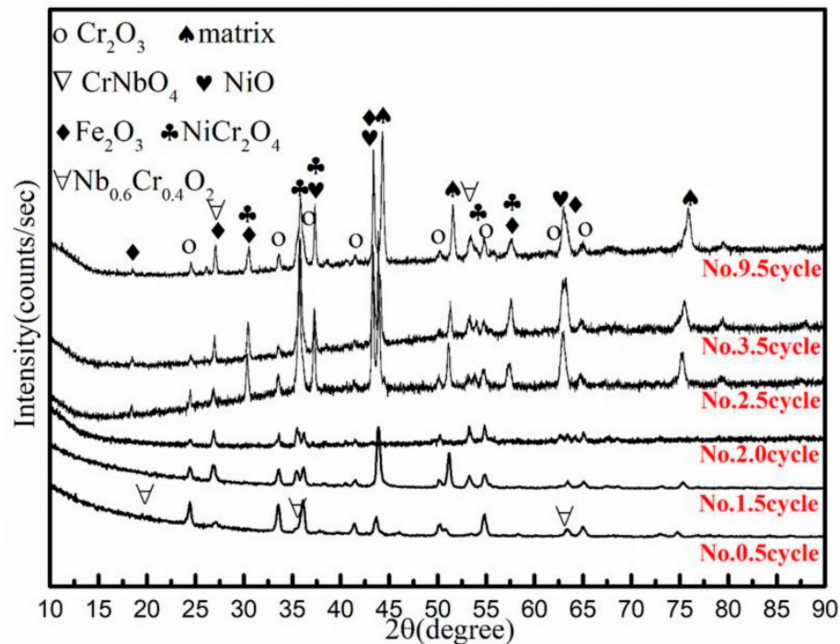

Figure 4. XRD results of the corrosion products remaining on the sample surface (No. 0.5, 1.5, 2.5, 3.5, 9.5 cycle) and spalling corrosion product powder filtered from 3.5%NaCl solution after No. 2 cycle.

3.3. Morphologies of the Oxides

The SEM surface morphologies of the corrosion oxides at different cycles are shown in Figure 5a–e. The EDS analysis of the oxides is shown in Table 2. At the No. 0.5 cycle, a dense and convex Cr_2O_3 film formed on the surface of the specimen (point 1). After the No. 1.5 cycle, the oxide film formed lots of defects, which became loose and began spalling, with many holes on the spalling surface. Combined with the EDS and XRD analysis, the oxides in the spalling areas were mainly composed of NiO and Fe_2O_3 with a small amount of Al_2O_3, while the oxide of unpeeled areas was Cr_2O_3 (point 2–4). The morphologies of the oxide films changed to more complicated triple layers after the No.2.5 cycle. The oxides in the outer layer consisted of NiO and Fe_2O_3. The intermediate layer, which had crackle, was mainly NiO, while the white granular oxide was NiO mixed with a small amount of Fe_2O_3 (point 6). The inner layer with a small number of pores consisted of NiO and Fe_2O_3, with lots of Cr_2O_3 beside the pores (point 7). After the No.3.5 cycle, the morphologies of the oxide film did not change significantly compared with the No. 2.5 cycle, and the compositions of the oxide scales at point 5 and point 8 were similar. After a severe spalling, the oxide scales formed at the No.9.5 cycle were much denser than those formed before. The outer oxide layer was composed of NiO and Fe_2O_3 (point 9). On the inner oxide scale, the grains grew up gradually as the cycles increased, and cracks along the grain boundary expanded. It consisted of NiO (point 10), with a small amount of Nb-rich oxides beside the grain boundaries (point 11). From the surface morphologies of the oxides' film, we can see that the protective Cr_2O_3 layer formed after the 0.5 cycle disappeared after immersion in 3.5 NaCl solution. The GH4169 alloy suffered serious corrosion after the 1.5 cycle, and lots of corrosion oxides, including NiO and Fe_2O_3, formed on the specimens.

Table 2. The EDS results of points shown in Figure 5.

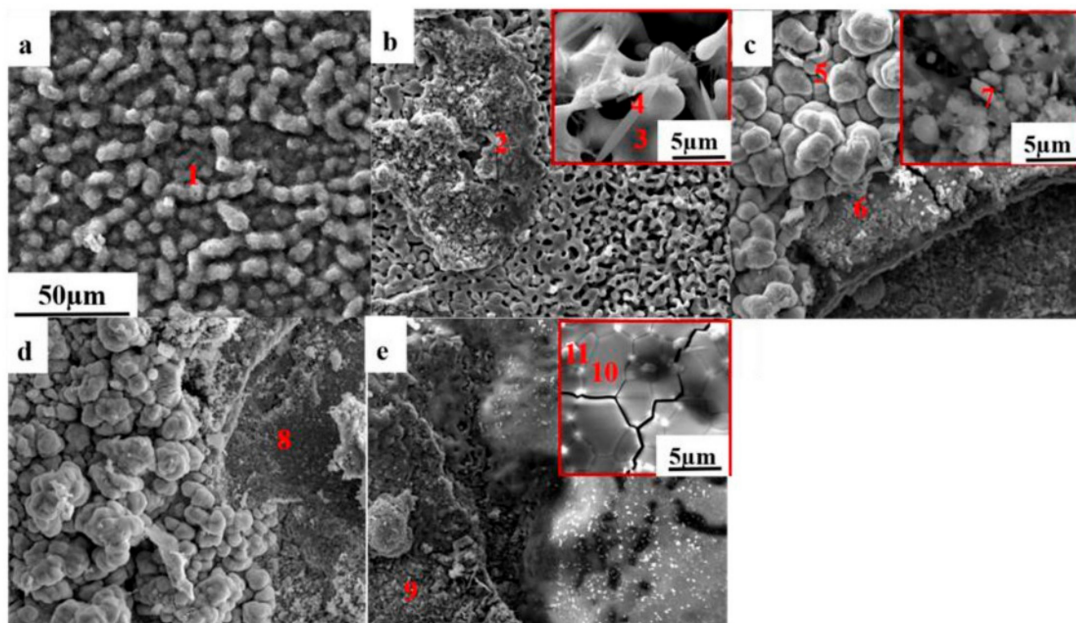| Element	Cr (at%)	Fe (at%)	Ni (at%)	Nb (at%)	Ti (at%)	Al (at%)	O (at%)
1	19.4	0.3	1.3	0.5	1.3	-	77.1
2	10.0	1.7	1.0	4.6	2.1	1.8	78.9
3	0.5	15.0	54.9	-	-	4.2	25.4
4	0.6	3.8	20.5	-	-	15.3	59.9
5	3.3	13.9	13.6	-	0.3	-	68.8
6	0.7	2.5	36.0	-	-	-	60.8
7	14.2	3.2	4.8	1.4	0.8	0.9	74.7
8	5.0	17.3	16.5	-	0.4	-	60.8
9	4.8	17.3	12.7	-	-	-	65.2
10	-	0.9	33.3	-	-	-	65.8
11	-	1.1	33.7	3.6	-	-	61.6

Figure 5. SEM surface morphologies (SEM, SEI) of corrosion products formed after (**a**) No. 0.5 cycle, (**b**) No. 1.5 cycle, (**c**) No. 2.5 cycle, (**d**) No. 3.5 cycle, and (**e**) No. 9.5 cycle.

Figure 6a–e shows the cross-section morphologies of the corrosion oxides at different cycles. The corresponding EDS analysis of the oxides is shown in Table 3. After the No. 0.5 cycle, a dense Cr_2O_3 formed on the surface (point 1). The internal oxidation of Al-rich oxides was detected as shown in Table 3 (point 3). A dense oxide formed at the interface between the outer oxide layer and the substrate, consisting of $CrNbO_4$ and a small amount of Ti and Nb oxides (point 2). After the No. 1.5 cycle, the oxides film had a multi layered structure. The outer layer with a few small holes was thicker than the No. 0.5 cycle, which mainly consisted of Cr_2O_3 (point 4). Spalling observations were made at the interface between oxides and based metals. Additionally, above the based metal, the inner layer with some cracks consisted of Cr, Nb, and Ti (point 5). The internal oxidation was more serious than the 0.5 cycle. After the No. 2.5 cycle, a thicker oxide scale formed with three layers, which shows that serous corrosion to the alloy at that time. A dense outmost layer consisting of NiO and Fe_2O_3, an intermediate layer with many large pores consisting of Cr_2O_3, and an innermost layer of $Nb_{0.6}Cr_{0.4}O_2$ and Nb and Ti -oxides (point 6–9) were formed. Meanwhile, internal oxidation was much more serious than before. From the No. 3.5 cycle to the No. 9.5 cycle, the oxide scales also consisted of three layers, and the phase composition changed slightly. However, as the test cycle increased, the number and size of the pores in the oxide scale increased. The thickness of the outset layer reduced, because of the spalling of the oxide scale. Actually, the internal oxidation was more and more serious.
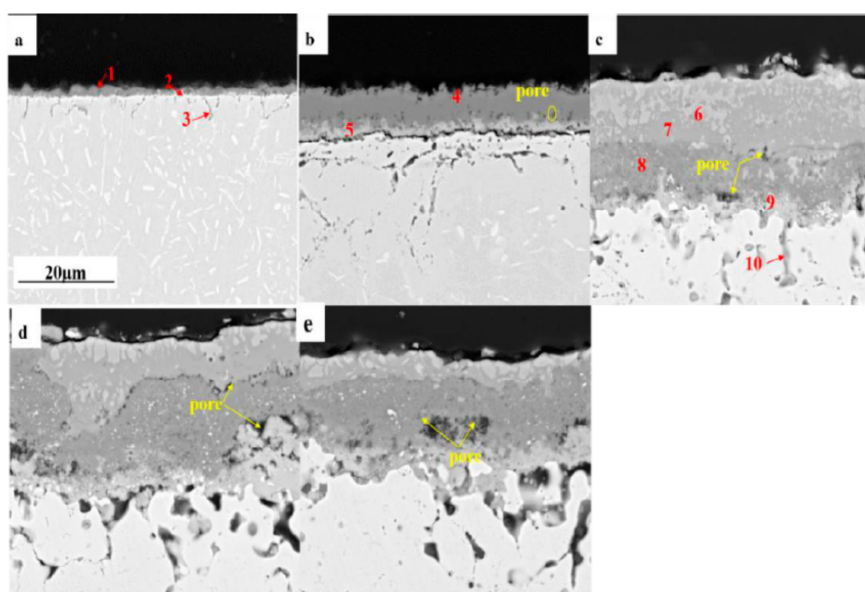
Figure 6. SEM cross-section morphologies (SEM, BEI) of corrosion products formed after (**a**) No. 0.5 cycle, (**b**) No. 1.5 cycle, (**c**) No. 2.5 cycle, (**d**) No. 3.5 cycle, and (**e**) No. 9.5 cycle.

Table 3. The EDS results of points shown in Figure 6.

Element	Cr (at%)	Fe (at%)	Ni (at%)	Nb (at%)	Ti (at%)	Al (at%)	O (at%)
1	17.5	1.7	0.5	3.0	4.0	2.4	70.8
2	6.2	4.9	34.8	9.8	1.0	1.5	41.8
3	9.4	13.0	34.7	2.1	1.6	10.7	28.6
4	33.6	-	-	-	-	-	66.4
5	27.2	-	-	12.9	3.7	1.7	54.5
6	0.5	4.1	41.6	-	-	-	53.8
7	0.9	24.1	16.4	-	-	-	58.6
8	31.8	0.5	1.5	-	0.3	-	65.8
9	10.5	0.9	3.1	13.4	3.7	1.3	67.2
10	1.3	13.4	51.0	-	-	5.5	28.8

The above experimental data show that the structures of oxide scales in the No. 1.5 cycle and No. 2.5 cycle changed more significantly. To better characterize the oxide scale formed on the superalloy GH4169 at this period, EMPA analyses were conducted. The elemental distributions in the oxide scale for the GH4169 samples oxidized under different cycles are shown in Figure 7. At the No.1.5 cycle, the outer layer was mainly composed of Cr-rich oxides. Beneath this layer, a mixed oxide layer with Nb and Ti-rich exists. The internal oxide was Al-rich oxide. Besides, Ni and Fe did not form a stable oxide. After 2.5 service cycles, the distributions of the corrosion product elements changed significantly. The outmost layer was composed mainly of Ni and Fe. The intermediate layer was composed of Cr. The innermost layer was rich in Nb and Ti. However, Ti and Nb oxides also diffuse into the outer layer. This transformation indicates that the corrosion products destroy the protection of Cr_2O_3. Large amounts of Ni and Fe oxides form in the outmost layer. This multi-oxide mixing can result in poor matching of oxide layers, thus causing the oxide layers to crack and spall. Therefore, the massive oxides spalled off from samples and weight loss became more and more serious.

Some compounds were not detected in XRD analysis, possibly due to the volume fractions of those compounds are less than 5% [22]. To better characterize the corrosion product, XPS analyses were conducted. The spectra of Cr2p, Ni2p, Fe2p, Ti2p, Nb3d, Al2p, Na1s, Cl2p and O1s acquired by XPS on the oxides film formed at different cycles are shown in Figure 8. The Ni 2p spectrum exhibits Ni^{2+} peeks at 855.9 and 861.5 related to NiO and $NiCr_2O_4$ [23,24]. As the cycles increased, the Ni-oxides

increased significantly, consistent with the XRD results. The Fe 2p spectrum exhibited a Fe^{2+} peek at 709.6 and a Fe^{3+} peek at 711.6 related to FeO and Fe_2O_3, respectively [25]. The spectra of Ti 2p, Nb3d, and Al2p corresponded to TiO_2, Al_2O_3, Nb_2O_5, and $CrNbO_4$, respectively. However, due to the low content of Ti, Nb, and Al in the superalloy, their peak signals were weak. Their phase could not be detected by XRD analyses. The spectra of O 1s results in two contributions originating from dissolved oxygen at 533.4 eV and oxide oxygen at 530.7 eV [26–28].
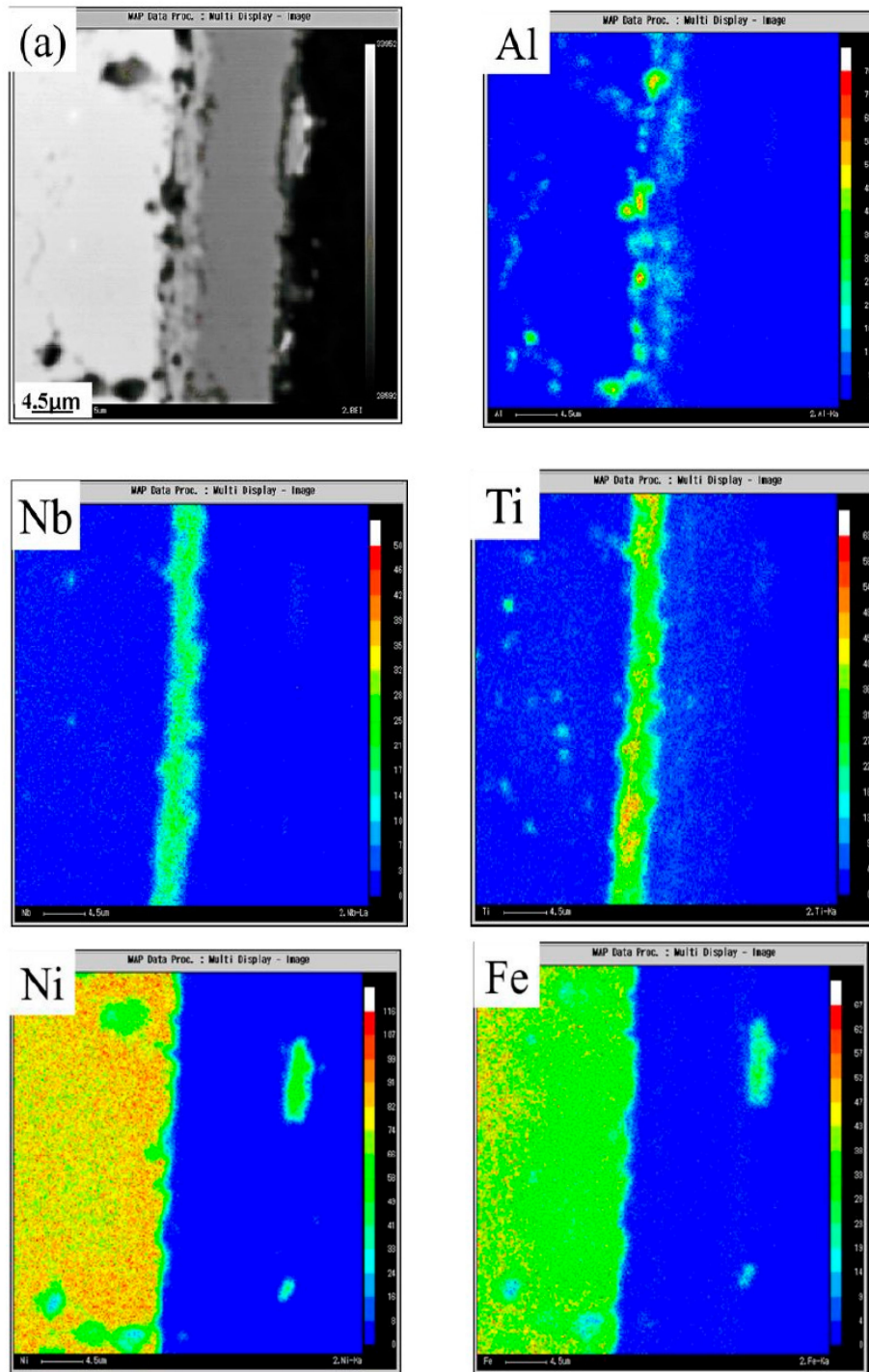
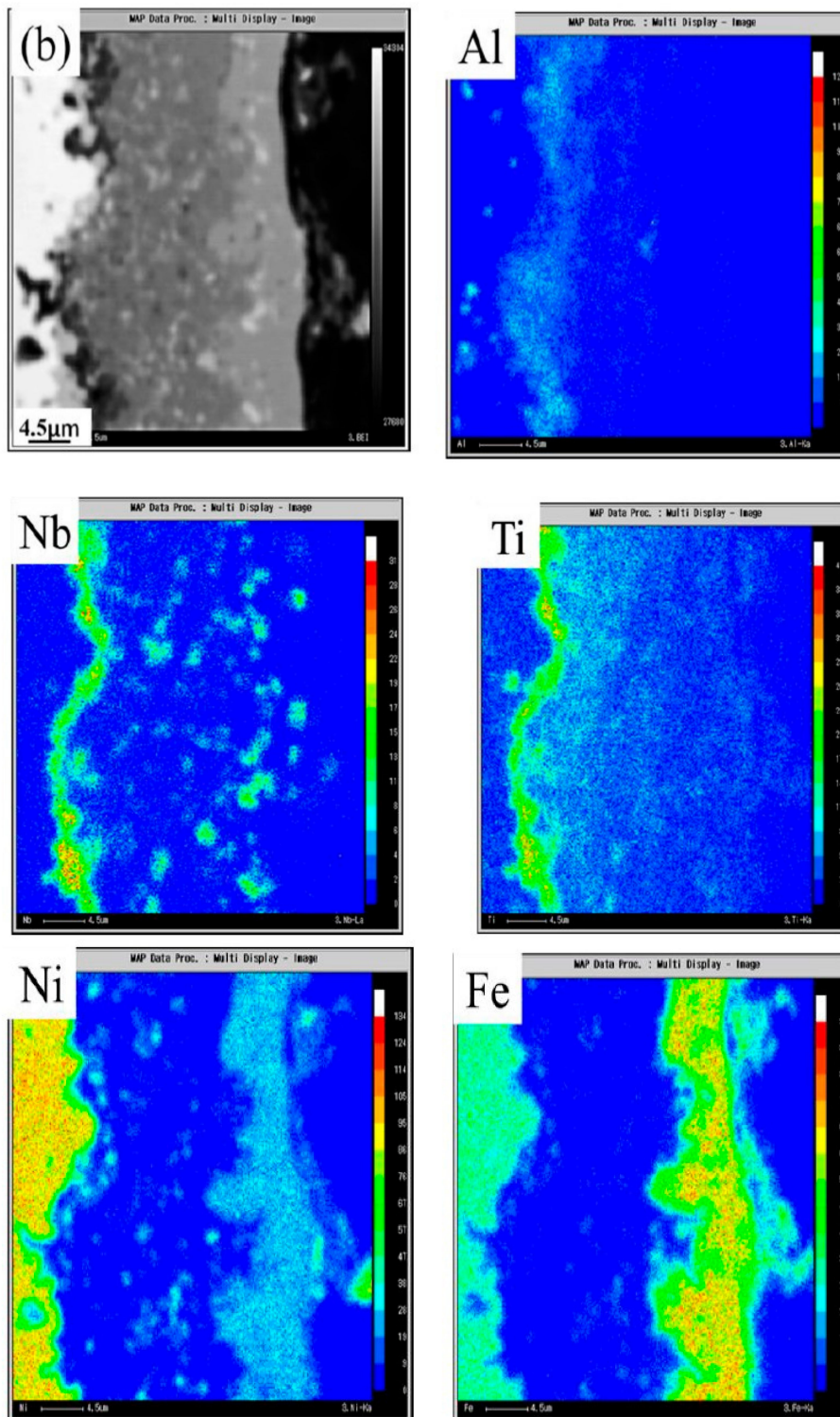**Figure 7.** *Cont.*
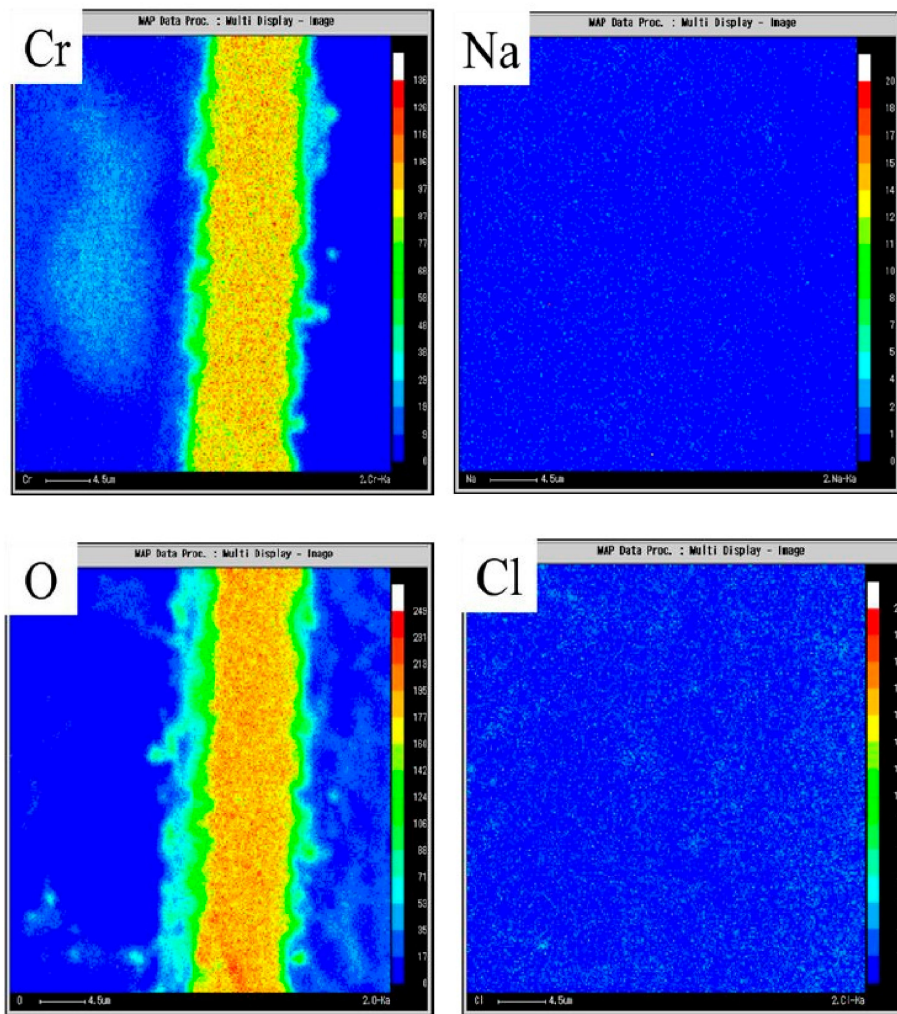
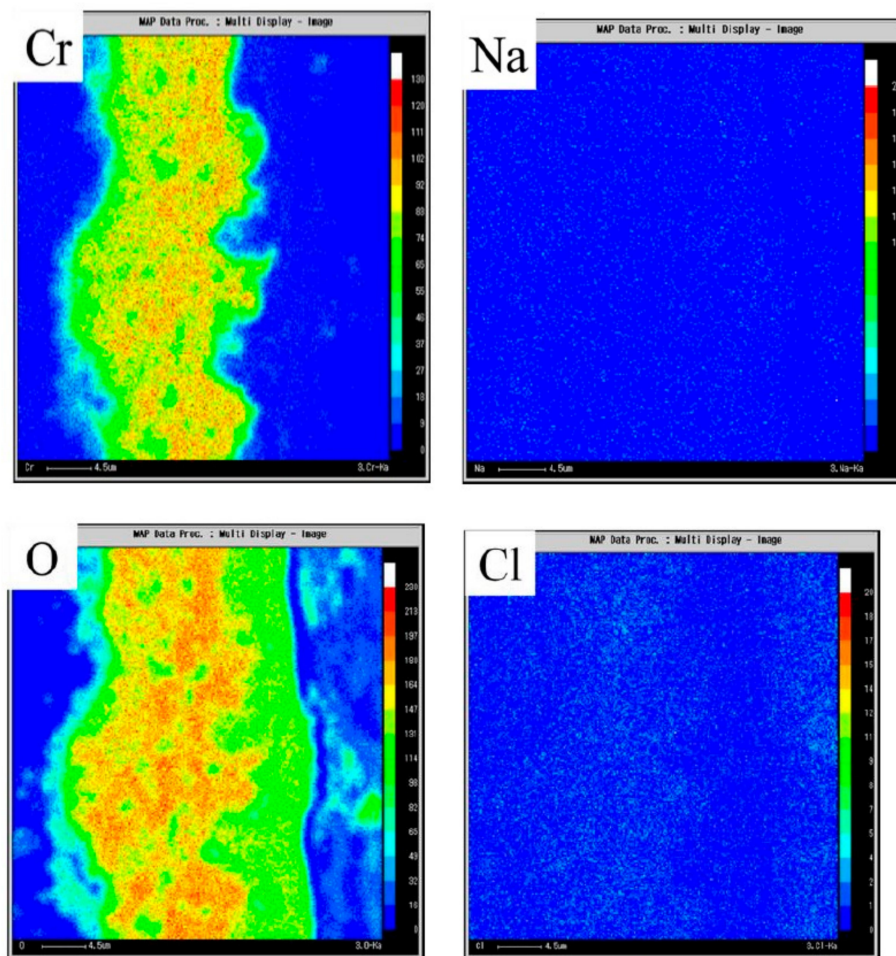**Figure 7.** *Cont.*

Figure 7. *Cont*.

Figure 7. EPMA images of corrosion products after (**a**) No. 1.5 cycle and (**b**) No. 2.5 cycle.

The above experimental results show that there is no NaCl or chlorides on the surface of samples after high temperature oxidation, which indicates that the chloride may be volatile. Therefore, volatile corrosion products piled on the quartz silks and tube inner wall above the furnace were collected from the suspended quartz silks and tube over the muffle furnace and analyzed by XPS. The spectra of Cr 2p, Fe 2p, Cl 2p, and Na 1s acquired by XPS on the collected volatile corrosion products are shown in Figure 9. The Cr2p spectrum exhibits that the products consisted of $Na_2Cr_2O_7$, Cr_2O_3, and $Na_2Cr_2O_4$. Meanwhile, the spectra of Na1s also shows the existence of $Na_2Cr_2O_7$ and $Na_2Cr_2O_4$. However, Cr_2O_3 and $Na_2Cr_2O_4$ cannot be volatilized at 900 °C, and they should be produced by decomposition of $Na_2Cr_2O_7$ [29]. The spectra of Ni2p indicates that the corrosion products contain NiO [24]. The spectra of Cl2p indicates that there is no Cl in the volatile corrosion products. Chlorides combined with oxygen form M_xO_y and Cl_2, which leads to chlorides not being detected [22,30].

The spectrum of Cr2p not only shows the existence of Cr_2O_3 and $NiCr_2O_4$ (576.8 and 586.4), but also characterizes the corrosion product of Cr^{6+} [31]. Considering the spectra of Na 1s, the corrosion products of Cr^{6+} may be $Na_2Cr_2O_7$ and $Na_2Cr_2O_4$. However, $Na_2Cr_2O_7$ is a highly volatile and decomposed compound at 900 °C, and Cr^{6+} in the oxide is considered to be $Na_2Cr_2O_4$. The spectrum of Cl2p indicates that there is no Cl compound in the corrosion product at all.
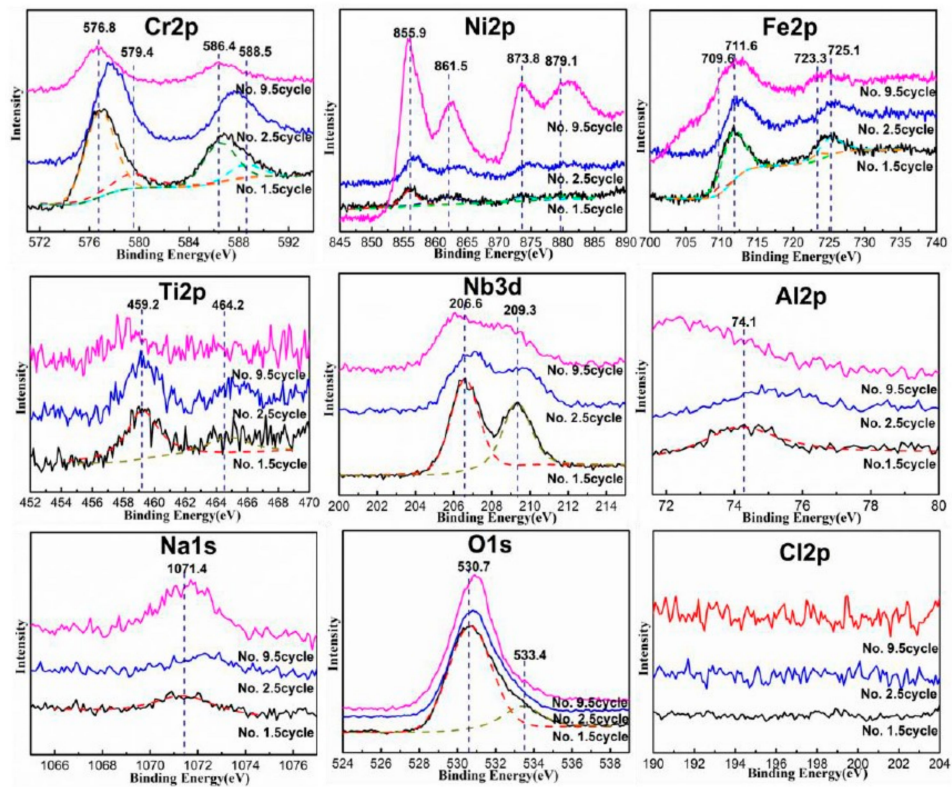
Figure 8. The XPS spectra of Cr 2p, Ni 2p, Fe 2p, Ti 2p, Nb 3d, Al 2p, Na 1s, O 1s, and Cl 2p of corrosion products formed after the No. 1.5 cycle, No. 2.5 cycle, and No. 9.5 cycle.
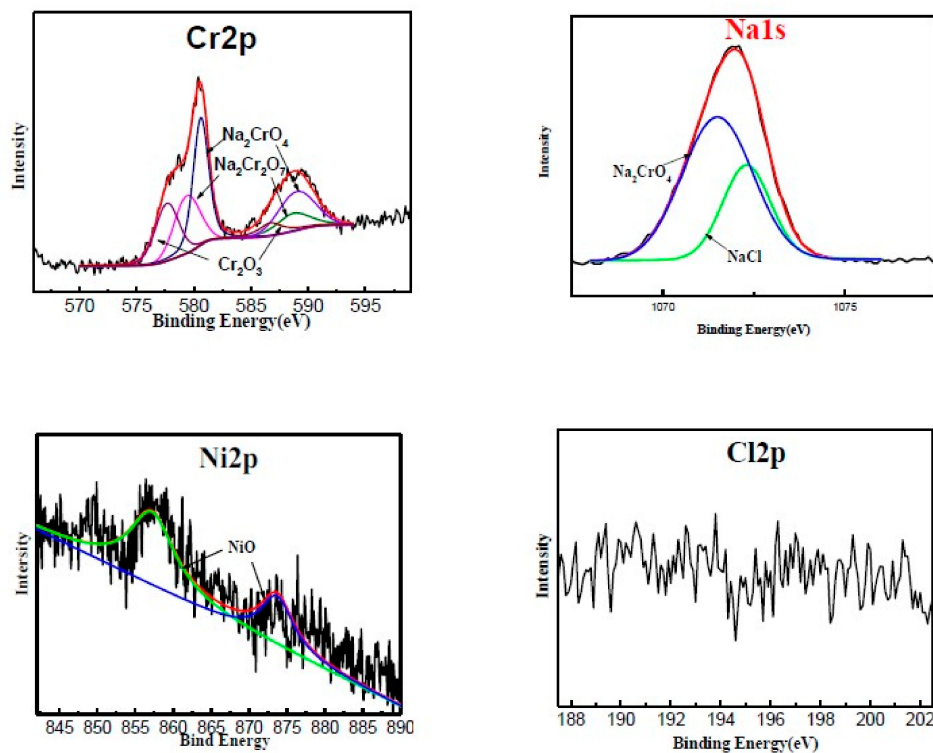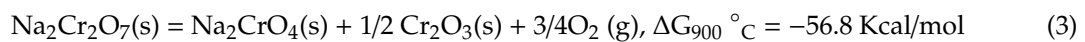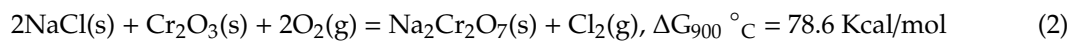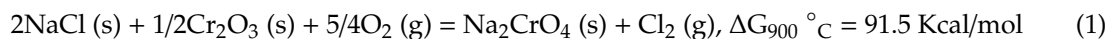

Figure 9. The XPS spectra of Cr 2p, Na 1s, Ni 2p, and Cl 2p of the collecting volatile corrosion products.
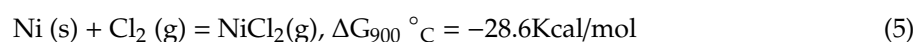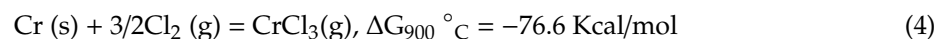
4. Discussion

4.1. The Mechanism of NaCl on Corrosion

The results obtained from this study clearly show that this alternating corrosion, including oxidation and solution immersion, increased the corrosion rate of GH4169. The obvious corrosion happened after immersion and during oxidation. After first oxidation at 900 °C, GH4169 formed a protective Cr_2O_3 layer, but it was destroyed after 1.5 cycle oxidation. The main reason should be that NaCl deposited on the surface of the sample reacted with Cr_2O_3 at 900 °C. The reactions of NaCl (s) with Cr_2O_3 are presented in Equations (1) and (2), in which the products of Na_2CrO_4, Cl_2 and $Na_2Cr_2O_7$ were formed. If NaCl is in the solid phase, the Gibbs free energy has a positive value. The same results were obtained in [32,33]. Although the theoretic calculation results show it is impossible for the reaction to happen, the reactions also are controlled by the products of Cl_2 and the partial pressure of Cl_2 [3]. If the partial pressure of Cl_2 is low enough, the reactions can happen [3]. In this work, the partial pressure of Cl_2 produced at equilibrium by Equation (1) at 900 °C is 2.99×10^{-5} atm, which was calculated by software HSC chemistry 6 (produced by OUTOKUMPU). This value of Equation (2) is 2.25×10^{-15} atm at the same temperature. Considering the Cl_2 in this work is produced in the oxide layer, the partial pressure should be low, which may be lower than the critical partial pressure of Cl_2. Combined with the experimental results, we think reaction (Equations (1) and (2)) can happen. However, $Na_2Cr_2O_7$ is unstable and prone to decomposition through the reaction of Equation (3) at 900 °C, which finally forms Na_2CrO_4 and Cr_2O_3 [33]. The Gibbs free energy of Equation (3) was calculated to be a negative value by software HSC chemistry 6, which means this reaction can happen easily. The XRD results testified this analysis. Therefore, NaCl destroyed the protective Cr_2O_3 layer.
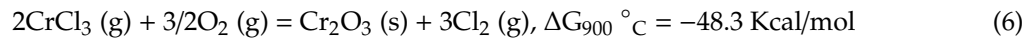
$$2NaCl~(s) + 1/2Cr_2O_3~(s) + 5/4O_2~(g) = Na_2CrO_4~(s) + Cl_2~(g),~\Delta G_{900~^\circ C} = 91.5~\text{Kcal/mol} \qquad (1)$$

$$2NaCl(s) + Cr_2O_3(s) + 2O_2(g) = Na_2Cr_2O_7(s) + Cl_2(g),~\Delta G_{900~^\circ C} = 78.6~\text{Kcal/mol} \qquad (2)$$

$$Na_2Cr_2O_7(s) = Na_2CrO_4(s) + 1/2~Cr_2O_3(s) + 3/4O_2~(g),~\Delta G_{900~^\circ C} = -56.8~\text{Kcal/mol} \qquad (3)$$

Meanwhile, Cl_2 and $Na_2Cr_2O_7$ have volatile properties, and the volatilization of them can lead to defects, such as holes, to form in the oxide scales. Defects can reduce the fracture toughness of scales, and it is difficult to release the stress in a thermal shock environment. After two cycles, we found that the oxides peeled off from the samples, which testified this. Moreover, Cl_2 (g) may penetrate into the substrate through the pores and cracks in the scale, and may reach the metal/scale interface [33,34]. Once the partial pressure of Cl_2 (g) increases at the interface between the metal and scale, the metal elements are unstable and can easily form the reaction by Equations (4) and (5) [35,36]:

$$Cr~(s) + 3/2Cl_2~(g) = CrCl_3(g),~\Delta G_{900~^\circ C} = -76.6~\text{Kcal/mol} \qquad (4)$$

$$Ni~(s) + Cl_2~(g) = NiCl_2(g),~\Delta G_{900~^\circ C} = -28.6\text{Kcal/mol} \qquad (5)$$

Chlorides ($CrCl_3$ and $NiCl_2$) may escape from the substrate/scale interface, and then the oxygen partial pressure is increased and the easy reaction of Equations (6) and (7) can occur [29,30]. The Gibbs free energies of Equations (4)–(7) were also negative, both of which mean reactions can happen. The volatilization of MCl_x causes more defects to form in the oxide scale, resulting in its spalling beingserious [33]. Therefore, the Cr_2O_3 layer was destroyed and lots of pores appeared under 900 °C at 1.5 cycles. The immersion in NaCl solution produced NaCl deposits on the surface of samples, which can be seen in Figure 2. NaCl reacted with oxides, which destroyed Cr_2O_3 and also promoted the formation of defects in the oxide scale. Subsequently, the sample was immersed in 3.5%NaCl aqueous solution, resulting in the dissolution of Na_2CrO_4 in the external and internal scales. Moreover, salt water entered the oxide layer to destroy the compactness of oxides. Meanwhile, the outward evaporation of H_2O caused the rapid dehydration of oxide layers and decreased the compactness of

oxide layers, too. The residual NaCl reacted again with the oxides to destroy the oxide layer more rapidly at high temperatures. Repeated alternation results in the disappearance of protective oxides, thus accelerating the corrosion of GH4169 alloy.

$$2CrCl_3 \text{ (g)} + 3/2O_2 \text{ (g)} = Cr_2O_3 \text{ (s)} + 3Cl_2 \text{ (g)}, \Delta G_{900} \,^{\circ}C = -48.3 \text{ Kcal/mol} \tag{6}$$

$$NiCl_2 \text{ (s)} + 1/2O_2 \text{ (g)} = NiO \text{ (s)} + Cl_2 \text{ (g)}, \Delta G_{900} \,^{\circ}C = -0.5 \text{ Kcal/mol} \tag{7}$$

4.2. Corrosion Mechanism

Schemes of the corrosion mechanism of GH4169 during the alternating high-temperature oxidation (900 °C) and normal temperature corrosion (3.5% NaCl solution, 30 ± 1 °C) are illustrated in Figure 10. A dense and protective Cr_2O_3 film was formed on the surface due to selective oxidation of Cr elements at the No. 0.5 cycle, as shown in Figure 5. Interface oxides of Nb_2O_5 can occur during phase reaction with Cr_2O_3, as shown in Equation (8), to form $CrNbO_4$, shown in the 0.5 cycle picture. After the immersion in 3.5% NaCl, a large amount of NaCl deposited on the oxide layer, as shown in Figure 2. Then, at the next oxidation, deposited NaCl reacted with the oxides, which destroyed the compact Cr_2O_3 and produced defects in the oxide scale as shown in the 1.5 cycle picture. The defects also promoted the spalling of the outer layer of Cr_2O_3 and accelerated the depletion of Cr. The corrosion products peeled off in the immersion solution, which was testified by the XRD result. The destruction of the continuous protective Cr_2O_3 scale produced the formation of Ni\Fe oxides. The defects provided channels for the diffusion of O_2, which promotes the oxidation of Nb at the substrate/scale interface. Ni was oxidized to NiO, and then reacted with Cr_2O_3 to form a compact spinel structure of the $NiCr_2O_4$, which could prevent more efficiently chlorination and oxidation. The interaction between them causes the reduction of Cr:Nb in interface oxides, as shown in Equation (8) [37,38]. There is not enough Cr_2O_3 to react with Nb_2O_5, thus $CrNbO_4$ transformed into $Nb_{0.6}Cr_{0.4}O_2$ [39].

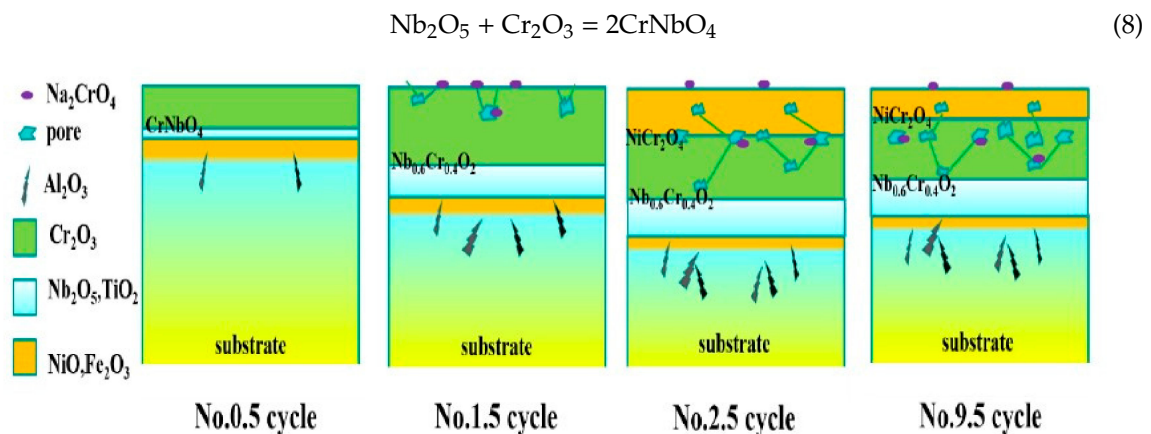$$Nb_2O_5 + Cr_2O_3 = 2CrNbO_4 \tag{8}$$

Figure 10. Schematic of GH4169 during the corrosion process under alternating oxidation at 900 °C and solution emersion.

A mixed outermost layer of NiO and Fe_2O_3 and an intermediate Cr_2O_3 layer were formed after the No. 2.5 cycle, as shown in Figure 7. The continuous Cr_2O_3 layer was destroyed, and then NiO and Fe_2O_3 formed. These mixed oxides piled on the surface of samples, so the oxide scale shows a more compact morphology than the No. 1.5 cycle (in Figure 5). The residual oxide scale is not protective. Ni and Fe can diffuse the outside of the Cr_2O_3 scale. The chemical reaction between NaCl and Cr_2O_3 results in changes of the structure and composition from the No. 1.5 cycle to the No. 2.5 cycle. At the same time, NiO reacts with Cr_2O_3 to form $NiCr_2O_4$ in the solid phase of Equation (9) [40–42]:

$$NiO + Cr_2O_3 = NiCr_2O_4 \tag{9}$$

From the No. 2.5 cycle to the No. 9.5 cycle, the outer oxide continuously peeled off, which was testified by SEM, XRD, and so on. The outward diffusion rate of the elements could not keep up with the spalling speed of the oxide scale, resulting in a decrease of the oxide scale thickness. Additionally, the inward diffusion of oxygen is increased by defects, and a large number of internal oxides are more and more serious under the outer scale [43,44]. The structure and composition of the outer layer of oxides scale changed significantly throughout the whole corrosion process. Otherwise, Nb with a higher valence than that of Ti is expected to decrease the concentration of oxygen vacancy and thus form a stable Nb and Ti-oxides interface layer [45].

5. Conclusions

GH4169 alloy suffered serious corrosion during the alternating at high-temperature oxidation and normal temperature corrosion. The deposited NaCl on the surface of samples after immersion reacted with Cr_2O_3 at the next oxidation, which is the main reason this serious corrosion was produced. The deposit, NaCl, reacted with Cr_2O_3 to form corrosion products, such as Cl_2, $Na_2Cr_2O_4$, $Na_2Cr_2O_7$, and $CrCl_3$, which consume Cr_2O_3 and promote the formation of defects inside the oxide scale. The outer oxide layer was changed from Cr_2O_3 to a mixed oxide of NiO and Fe_2O_3. After repeated iterations, the mixed oxides resulted in spalling of the oxide film because the fracture toughness of the corrosion scale was reduced.

Author Contributions: L.L. designed the research. Z.Y. performed the experiment. Z.Y., L.L., R.L., M.C., L.F., Y.L, S.G. and F.W. discussed and analyzed data. L.L. and R.L. wrote the manuscript. R.L and L.L. revised the paper.

Conflicts of Interest: The authors declare no conflict of interest.

References

1. Cruchley, S.; Evans, H.E.; Taylor, M.P.; Hardy, M.C.; Stekovic, S. Chromia layer growth on a Ni-based superalloy: Sub-parabolic kinetics and the role of titanium. *Corros. Sci.* **2013**, *75*, 58–66. [CrossRef]
2. Karabela, A.; Zhao, L.G.; Tong, J.; Simms, N.J.; Nicholls, J.R.; Hardy, M.C. Effects of cyclic stress and temperature on oxidation damage of a nickel-based superalloy. *Mater. Sci. Eng. A* **2011**, *528*, 6194–6202. [CrossRef]
3. Wang, J.W.; Zhang, C.Z.; Li, Z.H.; Zhou, H.X.; He, J.X.; Yu, J.C. Corrosion behavior of nickel-based superalloys in thermal storage medium of molten eutectic $NaCl\text{-}MgCl_2$ in atmosphere. *Sol. Energy Mater. Sol. Cells* **2017**, *164*, 146–155. [CrossRef]
4. Rajendran, R. Gas turbine coatings—An overview. *Eng. Failure Anal.* **2012**, *26*, 355–369. [CrossRef]
5. Zheng, L.; Maicang, Z.; Jianxin, D. Hot corrosion behavior of powder metallurgy Rene95 nickel-based superalloy in molten $NaCl\text{–}Na_2SO_4$ salts. *Mater. Des.* **2011**, *32*, 1981–1989. [CrossRef]
6. Mannava, V.; SambasivaRao, A.; Kamaraj, M.; Kottada, R.S. Influence of Two Different Salt Mixture Combinations of $Na_2SO_4\text{-}NaCl\text{-}NaVO_3$ on Hot Corrosion Behavior of Ni-Base Superalloy Nimonic263 at 800 °C. *J. Mater. Eng. Perform.* **2019**, *28*, 1077–1093. [CrossRef]
7. Chiou, M.S.; Yeh, A.C.; Jian, S.R.; Kuo, C.M. High Temperature Oxidation Behavior of CM-247LC Nickel Base Superalloy. *Adv. Mater. Res.* **2014**, *922*, 61–66. [CrossRef]
8. Deng, W.-F.; Luo, H.-L.; Li, S.-P.; Zhou, T.-T. Isothermal Oxidation Behavior of a Cast Ni3Al-Base Superalloy MX 246A. *J. Iron Steel Res. Int.* **2007**, *14*, 59–65. [CrossRef]
9. Gao, S.; Hou, J.S.; Yang, F.; Wang, C.S.; Zhou, L.Z. High Temperature Oxidation Behaviors of Two Cast Ni-based Superalloys. *Rare Met. Mat. Eng.* **2019**, *48*, 960–966.
10. Nofz, M.; Dorfel, I.; Sojref, R.; Neumann, R.S. Microstructure of Bare and Sol-Gel Alumina-Coated Nickel-Base Alloy Inconel 625 After Long-Term Oxidation at 900 degrees C. *Oxid. Met.* **2019**, *91*, 395–416. [CrossRef]
11. Cao, J.D.; Zhang, J.S.; Hua, Y.Q.; Rong, Z.; Chen, R.F.; Ye, Y.X. High temperature oxidation behavior of Ni-based superalloy GH586 in air. *Rare Met.* **2017**, *36*, 878–885. [CrossRef]

12. Mahesh, R.A.; Jayaganthan, R.; Prakash, S. Oxidation behaviour of selected Ni- and Fe- based superalloys in air at 900 °C under cyclic conditions. *Trans. Indian Inst. Met.* **2008**, *61*, 45–49. [CrossRef]

13. Al-Hatab, K.A.; Al-Bukhaiti, M.A.; Krupp, U.; Kantehm, M. Cyclic Oxidation Kinetics and Oxide Scale Morphologies Developed on the IN600 Superalloy. *Oxid. Met.* **2011**, *76*, 385–398. [CrossRef]

14. Lu, X.D.; Guo, C.A.; Wang, J.; Ma, S.W. Cyclic Oxidation Behaviour of a Ni-Based Alloy at 900 °C. *Appl. Mech. Mater.* **2011**, *80–81*, 51–54. [CrossRef]

15. Salehi Doolabi, M.; Ghasemi, B.; Sadrnezhaad, S.K.; Habibollahzadeh, A.; Jafarzadeh, K. Hot corrosion behavior and near-surface microstructure of a "low-temperature high-activity Cr-aluminide" coating on inconel 738LC exposed to Na_2SO_4, $Na_2SO_4 + V_2O_5$ and $Na_2SO_4 + V_2O_5 + NaCl$ at 900 °C. *Corros. Sci.* **2017**, *128*, 42–53. [CrossRef]

16. Weng, F.; Yu, H.; Wan, K.; Chen, C. The influence of Nb on hot corrosion behavior of Ni-based superalloy at 800 °C in a mixture of Na_2SO_4–NaCl. *J. Mater. Res.* **2014**, *29*, 2596–2603. [CrossRef]

17. Cao, J.; Zhang, J.; Hua, Y.; Chen, R.; Li, Z.; Ye, Y. Microstructure and hot corrosion behavior of the Ni-based superalloy GH202 treated by laser shock processing. *Mater. Charact.* **2017**, *125*, 67–75. [CrossRef]

18. Liu, G.M.; Yu, F.; Tian, J.H.; Ma, J.H. Influence of pre-oxidation on the hot corrosion of M38G superalloy in the mixture of Na 2 SO 4 –NaCl melts. *Mater. Sci. Eng. A* **2006**, *496*, 40–44. [CrossRef]

19. Fantozzi, D.; Matikainen, V.; Uusitalo, M.; Koivuluoto, H.; Vuoristo, P. Chlorine-induced high temperature corrosion of Inconel 625 sprayed coatings deposited with different thermal spray techniques. *Surf. Coat. Tech.* **2016**, *318*, 233–243. [CrossRef]

20. Chen, L.; Hao, L.; Huang, C.; Yang, B.; Du, L.; Zhang, W. Hot corrosion behavior of porous nickel-based alloys containing molybdenum in the presence of NaCl at 750 °C. *Eng. Failure Anal.* **2017**, *79*, 245–252. [CrossRef]

21. Pradhan, D.; Mahobia, G.S.; Chattopadhyay, K.; Singh, V. Effect of surface roughness on corrosion behavior of the superalloy IN718 in simulated marine environment. *J. Alloys Compd.* **2018**, *740*, 250–263. [CrossRef]

22. Yan, L.; Fang, X.; Zhang, S.; Xue, F. Microstructure evolution of FeNiCr alloy induced by stress-oxidation coupling using high temperature nanoindentation. *Corros. Sci.* **2018**, *135*, 192–196.

23. Siemensmeyer, B.; Schultze, J.W. XPS and UPS studies of gas-phase oxidation, electrochemistry and corrosion behaviour of Ti and Ti5Ta. *Surf. Interface Anal.* **1990**, *16*, 309–314. [CrossRef]

24. Šarić, I.; Peter, R.; Kavre, I.; Badovinac, I.J.; Petravić, M. Oxidation of nickel surfaces by low energy ion bombardment. *Nucl. Instrum. Methods Phys. Res. Sect. B* **2015**, *371*, 286–289. [CrossRef]

25. Biesinger, M.C.; Payne, B.P.; Lau, L.W.M.; Gerson, A.; Smart, R.S.C. X-ray photoelectron spectroscopic chemical state quantification of mixed nickel metal, oxide and hydroxide systems. *Surf. Interface Anal.* **2009**, *41*, 324–332. [CrossRef]

26. Feng, S.; Man, K.T.; Pohl, M.M.; Radnik, J.; Brückner, A.; Zhang, S.; Beller, M. Nano-iron oxide-catalyzed selective oxidations of alcohols and olefins with hydrogen peroxide. *J. Mol. Catal. A Chem.* **2008**, *292*, 28–35.

27. Sasahara, A.; Tomitori, M. XPS and STM study of Nb-doped $TiO_2(110)$-(1×1) surfaces. *J. Phys. Chem. C* **2013**, *117*, 17680–17686. [CrossRef]

28. Ho, S.F.; Contarini, S.; Rabalais, J.W. Ion-beam-induced chemical changes in the oxyanions (Moyn-) and oxides (Mox) where M = chromium, molybdenum, tungsten, vanadium, niobium and tantalum. *J. Phys. Chem.* **1987**, *91*, 4779–4788. [CrossRef]

29. Mannava, V.; Rao, A.S.; Paulose, N.; Kamaraj, M.; Kottada, R.S. Hot corrosion studies on Ni-base superalloy at 650°C under marine-like environment conditions using three salt mixture ($Na^2SO^4+NaCl+NaVO_3$). *Corros. Sci.* **2016**, *105*, 109–119. [CrossRef]

30. Bai, Y.; Hua, Y.; Rong, Z.; Ye, Y.; Xue, Q.; Liu, H.; Chen, R. Cyclic Oxidation Resistance of In718 Superalloy Treated by Laser Peening. *J. Wuhan Univ. Technol.-Mater. Sci. Ed.* **2015**, *30*, 808–812. [CrossRef]

31. Wu, C.; Feng, W.; Chen, L.; Huang, X. X-ray diffraction and X-ray photoelectron spectroscopy analysis of Cr-doped spinel $LiMn_2O_4$ for lithium ion batteries. *Solid State Ionics* **2002**, *152*, 335–339. [CrossRef]

32. Shu, Y.; Wang, F.; Wu, W. Synergistic effect of NaCl and water vapor on the corrosion of 1Cr-11Ni-2W-2Mo-V steel at 500–700 °C. *Oxid. Met.* **1999**, *51*, 97–110. [CrossRef]

33. Shu, Y.; Wang, F.; Wu, W. Corrosion behavior of pure Cr with a solid NaCl deposit in O_2 plus water vapor. *Oxid. Met.* **2000**, *54*, 457–471. [CrossRef]

34. Gong, X.; Chen, R.R.; Yang, Y.H.; Wang, Y.; Ding, H.S.; Guo, J.J.; Su, Y.Q.; Fu, H.Z. Effect of Mo on microstructure and oxidation of NiCoCrAlY coatings on high Nb containing TiAl alloys. *Appl. Surf. Sci.* **2017**, *431*, 81–92. [CrossRef]

35. Zhang, H.; Yuan, L.; Xiang, C.; Zhang, H.; Li, Y. Microstructural homogenization and high-temperature cyclic oxidation behavior of a Ni-based superalloy with high-Cr content. *J. Alloys Compd.* **2017**, *727*, 410–418. [CrossRef]

36. Hofmeister, M.; Klein, L.; Miran, H.; Rettig, R.; Virtanen, S.; Singer, R.F. Corrosion behaviour of stainless steels and a single crystal superalloy in a ternary LiCl–KCl–CsCl molten salt. *Corros. Sci.* **2015**, *90*, 46–53. [CrossRef]

37. Cruchley, S.; Taylor, M.P.; Ding, R.; Evans, H.E.; Child, D.J.; Hardy, M.C. Comparison of Chromia Growth Kinetics in a Ni-based Superalloy, With and without Shot-peening. *Corros. Sci.* **2015**, *100*, 242–252. [CrossRef]

38. Zhang, P.; Li, Y.; Chen, Z.; Zhang, J.; Shen, B. Oxidation response of a vacuum arc melted NbZrTiCrAl refractory high entropy alloy at 800–1200 °C. *Vacuum* **2019**, *162*, 20–27. [CrossRef]

39. Yao, D.; Zhou, C.; Yang, J.; Chen, H. Experimental studies and modeling of the oxidation of multiphase niobium-base alloys. *Corros. Sci.* **2009**, *51*, 2619–2627. [CrossRef]

40. Calvarin, G.; Molins, R.; Huntz, A.M. Oxidation Mechanism of Ni—20Cr Foils and Its Relation to the Oxide-Scale Microstructure. *Oxid. Met.* **2000**, *53*, 25–48. [CrossRef]

41. Gao, R.; Ye, X.X.; Yan, S.; Lu, Y.L.; Jiang, L.; Li, Z.J.; Zhou, X.T. Effects of tungsten content on the high-temperature oxidation behavior of Ni-xW-6Cr alloys. *Corros. Sci.* **2019**, *149*, 87–99. [CrossRef]

42. Jiang, J.F.; Xiao, G.F.; Wang, Y.; Liu, Y.Z. High temperature oxidation behavior of the wrought Ni-based superalloy GH4037 in the solid and semi-solid state. *J. Alloy Compd.* **2019**, *784*, 394–404. [CrossRef]

43. Saladi, S.; Menghani, J.; Prakash, S. A Study on the Cyclic Oxidation Behavior of Detonation-Gun-Sprayed Ni-5Al Coatings on Inconel-718 at 900 °C. *J. Mater. Eng. Perform.* **2014**, *23*, 4394–4403. [CrossRef]

44. Saber, D.; Emam, I.S.; Abdel-Karim, R. High temperature cyclic oxidation of Ni based superalloys at different temperatures in air. *J. Alloys Compd.* **2017**, *719*, 133–141. [CrossRef]

45. Lin, J.P.; Zhao, L.L.; Li, G.Y.; Zhang, L.Q.; Song, X.P.; Ye, F.; Chen, G.L. Effect of Nb on oxidation behavior of high Nb containing TiAl alloys. *Intermetallics* **2011**, *19*, 131–136. [CrossRef]